

Research Article

CO₂ Permeability Analysis of Caprock Containing a Single Fracture Subject to Coupled Thermal-Hydrromechanical Effects

Qian Yin,¹ Hongwen Jing,¹ Haijian Su,¹ and Huidong Wang²

¹State Key Laboratory for Geomechanics and Deep Underground Engineering, China University of Mining and Technology, Xuzhou 221116, China

²College of Architecture and Civil Engineering, Beijing University of Technology, Beijing 100124, China

Correspondence should be addressed to Qian Yin; jeryin@foxmail.com

Received 20 January 2017; Accepted 26 February 2017; Published 28 March 2017

Academic Editor: Sandro Longo

Copyright © 2017 Qian Yin et al. This is an open access article distributed under the Creative Commons Attribution License, which permits unrestricted use, distribution, and reproduction in any medium, provided the original work is properly cited.

Coupled THM (thermal-hydrromechanical) processes have become increasingly important in studying the issues affecting subsurface flow systems. CO₂ permeability of the fracture in caprock is a key factor that affects sealing efficiency of caprock. A new model associated with coupled THM processes that shows a good reliability was derived. Then, based on the COMSOL multiphysics software, a series of numerical calculations were performed on caprock models with a single fracture subject to coupled THM effects. Transmissivity of the fracture as a function of fracture angle, overburden pressure, fluid pressure difference, injected CO₂ temperature, and the initial fracture aperture was elucidated, respectively. Average transmissivity of the fracture undergoes an increase by 1.74 times with the fracture angle (45°–90°), 2–3 orders of magnitude with the fluid pressure difference (5–30 MPa), and 4–5 orders of magnitude with the initial fracture aperture (0.05–0.5 mm), while it decreases by 3–4 orders of magnitude as overburden pressure increases from 30 to 80 MPa. Injected CO₂ temperature has a small impact on the fracture permeability. This work provides an alternative tool to enrich the numerical modeling for the assessment of CO₂ caprock sealing efficiency.

1. Introduction

To address the increasing concerns regarding carbon dioxide emission and its impact on climate change, CO₂ geological sequestration has become a promising approach [1–5]. To reduce the atmosphere emissions, a large amount of CO₂ is injected into the geological storage reservoirs, as shown in Figure 1, which may be gradually accumulated at the bottom of caprocks and lead to stress field changes in caprock. However, if the reservoir pressure is high enough to cause mechanical failure in caprock and connected pathways are created through fractures, a potential hazard of CO₂ leakage will occur [6–8].

Research on subsurface CO₂ flow systems involves thermal (T), hydrodynamic (H), and mechanical (M) processes. In fact, these processes are interrelated and affect each other and are referred to as “coupled THM effects” [9], which has a significant influence on sealing efficiency of caprock [10]. Permeability of the fracture in caprock is the key safety issue for CO₂ geological sequestration in storage reservoirs.

Numerical simulations have been widely used to evaluate CO₂ multiphase flow, diffusion, geomechanics, and chemical reactions during CO₂ injection and storage. In the multiphase flow research field, TOUGH2 codes, which consider the cross-coupling of TH and THC processes for multiphase flow, were developed [11]. Two existing well-established codes, TOUGH2 and FLAC^{3D}, have been adopted as a pragmatic approach for modeling coupled THM processes [12]. Besides, TOUGHREACT and FLAC^{3D} have been linked together to simulate coupled THMC processes [13]. A novel fully coupled flow and geomechanics model TOUGH2-EGS in enhanced geothermal reservoirs based on average Navier equation was developed [14]. FEHM finite element codes were also applied to simulate coupled THM processes in subsurface fractured media [15]. A mechanical simulation module TOUGH2Biot, which was based on the extended Biot consolidation model and finite element method, was developed and applied to CO₂ sequestration simulation [9]. COMSOL multiphysics software, which can be used to simulate ground water flow

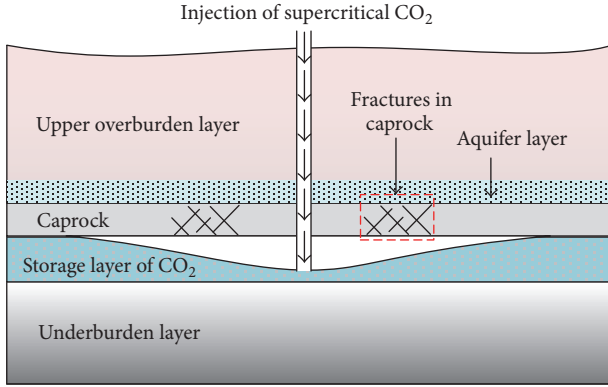


FIGURE 1: Schematic of CO₂ injection in the presence of fractures within the caprock layer.

subject to coupled THM effects if a suitable template and relationship between the coupled processes are constructed, has been widely employed recently [16]. In previous studies, even though substantial efforts have been devoted to estimation and prediction of the CO₂ sequestration performance, the theory for fracture permeability in caprock and the corresponding sealing efficiency of caprock have so far not been fully developed due to dual complexity of THM coupled processes and geological conditions.

This paper is organized as follows. A new coupled thermal-hydromechanical model for CO₂ flow through a single fracture in caprock was first derived. The governing equations were linked with COMSOL multiphysics software, and the reliability of the model was verified using a sample problem. Finally, several numerical calculations on caprock models with a single fracture subject to coupled THM effects were performed, and CO₂ permeability of the fracture with respect to different fracture angle, overburden pressure, fluid pressure difference, injected CO₂ temperature, and initial aperture was, respectively, evaluated. In this study, these models were calculated under simplified conditions of single-phase flow and heat conduction alone in thermal field for brevity.

2. Governing Equations

In the following, a set of field equations are defined which govern the deformation of caprock matrix, the fluid flow through the fracture, and the heat conduction process. These derivations are obtained based on the following assumptions. (i) Caprock matrix is a kind of homogeneous, isotropic, and elastic continuum. (ii) Strains are much smaller than the length scale. (iii) No crack propagation happens to the caprock matrix and no dislocation occurs between the matrix blocks. (iv) The matrix is impermeable, and CO₂ flows through the fracture alone. The fluid flow behavior can be described using Darcy's law. (v) Heat effect induced by fluid flow through the fracture is negligible, and heat conduction within the matrix follows Fourier's law. (vi) Density and viscosity of the supercritical CO₂ vary with the temperature and pressure.

2.1. Governing Equation for Caprock Matrix Deformation. To elucidate the mechanical response of caprock containing fractures under coupled THM effects and to evaluate the permeability of fractures within the caprock, a typical mechanical model is built and shown in Figure 2(a). The lower boundary of the model is displacement constraint. Due to continuous CO₂ injection, pressure is built up at the lower boundary of the caprock. Buried depth of caprock provides a vertical pressure of q at the upper boundary, and both lateral sides are subjected to an equal pressure of q_l . Then, stress analysis of a microunit chosen from the caprock matrix (the dashed region in Figure 2(a)) is conducted, as shown in Figure 2(b). T_0 and T_C , respectively, denote the temperature of caprock matrix and injected CO₂. For a homogeneous, isotropic, and elastic medium, the strain-displacement relation of the matrix can be expressed as

$$\varepsilon_{ij}^T + \varepsilon_{ij}^q = \frac{1}{2} (u_{i,j}^T + u_{i,j}^q + u_{j,i}^T + u_{j,i}^q), \quad (1)$$

where ε^T and ε^q are component of the total strain tensor produced by temperature and applied load, respectively. u^T and u^q are the component of displacement. The equilibrium equation is defined as

$$\sigma_{ij,i}^T + \sigma_{ij,i}^q + f_j = 0, \quad (2)$$

where σ^T and σ^q denote the component of the total stress tensor produced by the temperature and applied load. f_j denotes the component of the body force.

Then, the constitutive relation for the deformed caprock matrix becomes

$$\sigma_{ij} = 2G\varepsilon_{ij} + \lambda\varepsilon_{kk}\delta_{ij} - \frac{\alpha E \Delta T}{1 - 2\nu} \delta_{ij}, \quad (3)$$

where λ and G are Lamé constants, ν is Poisson's ratio, E is Young's modulus, ΔT is the temperature variation, α is the thermal expansion coefficient of rock, and δ_{ij} is the Kronecker delta. Combination of (1)–(3) yields the equilibrium differential equation, written as

$$G\nabla^2 u_i + (\lambda + G) u_{j,jj} - \frac{\alpha E}{1 - 2\nu} \Delta T_{,i} + f_i = 0. \quad (4)$$

Equation (4) is the governing equation for caprock deformation, from which stress distribution of caprock can be calculated.

Natural fractures are often subjected to field stresses or mechanical displacements, which have a direct influence on the fracture aperture and hence the permeability of the fractured rock. The fracture aperture may increase due to shear dilation [20–23] or decrease in response to the normal loads [24–27]. At present, relations between fracture permeability and the applied normal loads are clear and have been widely accepted by scholars in the field. However, no unified understanding has been obtained for effect of shear stress on the fracture permeability. Therefore, in this study, the role of shear stress on CO₂ flows through the fracture is not taken into account.

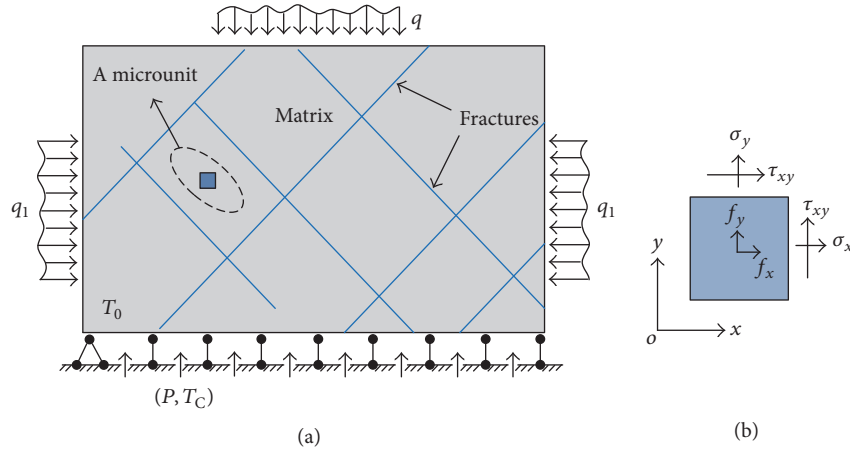


FIGURE 2: Mechanical model of caprock containing fractures.

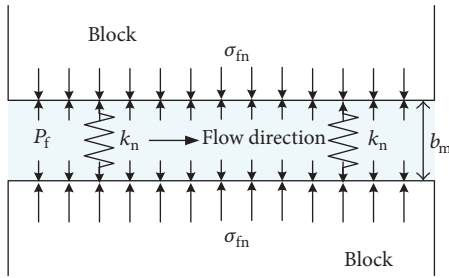


FIGURE 3: Mechanical model of the fracture.

Figure 3 shows a typical mechanical model of a fracture. When CO_2 flows in the fracture, a fluid pressure of P_f is applied on the fracture surface. σ_{fn} and k_n , respectively, denote the normal contact stress and normal stiffness between two blocks.

According to the definition of effective stress in porous media, the effective stress in the fracture can be written as

$$\sigma_{fne} = \sigma_{fn} - P_f. \quad (5)$$

By using the distinct element code of UDEC, a simple description of the relation between σ_{fne} and the mechanical aperture b_m was given [28], as indicated by the solid lines in Figure 4. In the range of residual aperture b_{res} and maximum aperture b_{max} , σ_{fne} is linearly proportional to b_m , written as

$$b_m = b_{m0} - \frac{\sigma_{fne}}{k_n}, \quad (6)$$

where b_{m0} is the initial fracture aperture with no applied load.

From Figure 4, when $\sigma_{fne} > 0$, fracture closure happens, and with the increase of σ_{fne} , b_m continues to decrease linearly until b_{res} . When $b_m = b_{res}$, the fracture aperture keeps a constant value which no longer depends on σ_{fne} . When $\sigma_{fne} < 0$, b_m increases with the increase of $-\sigma_{fne}$ until b_{max} . When $b_m = b_{max}$, b_m remains unchanged.

In this study, for $\sigma_{fne} < 0$, the linear relation between σ_{fne} and b_m in Figure 4 is still adopted to describe the variation

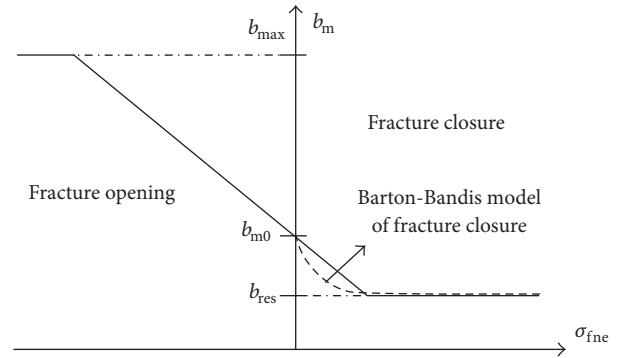


FIGURE 4: Fracture aperture as a function of the effective normal stress.

of b_m . However, for $\sigma_{fne} > 0$, the Barton-Bandis equation is utilized to evaluate the fracture closure behavior, as shown by the dashed line in Figure 4. The equation is a kind of hyperbolic model put forward by Bandis et al. [29] through experiments to describe the fracture deformation with the effective normal stress, written as

$$\Delta V_j^c = \frac{\sigma_{fne}}{k_{n0} + \sigma_{fne}/b_{m0}}, \quad (7)$$

where ΔV_j^c is the fracture closure and k_{n0} is the initial normal stiffness with no applied load.

According to (7), the normal stiffness of the fracture can be determined as

$$k_n = \frac{\partial \sigma_{fne}}{\partial V_j^c} = k_{n0} \left(1 - \frac{\sigma_{fne}}{k_{n0} b_{m0} + \sigma_{fne}} \right)^{-2} \quad (8)$$

and the fracture aperture can be described as

$$b_m = b_{m0} - \Delta V_j^c. \quad (9)$$

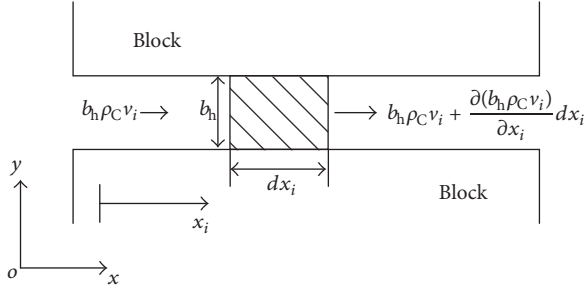


FIGURE 5: Hydraulic model of fluid flow through a fracture.

2.2. Governing Equation for Fluid Flow. For the two dimensional model described in Figure 2, fluid flow through the fracture can be solved as a one-dimensional problem. Figure 5 presents the hydraulic calculation model for a microunit in the fracture i .

In terms of the local coordinate system of a fracture, for continuously saturated fluid flow, the mass conservation equation regardless of the source sink can be written as

$$-\frac{\partial(\rho_C v_i b_h)}{\partial x_i} dx_i = \frac{\partial(\rho_C b_h dx_i)}{\partial t}, \quad (10)$$

where ρ_C is the density of CO_2 , v_i denotes the flow velocity, t is the time, and b_h is the equivalent hydraulic aperture.

According to Darcy's law, v_i is given by

$$v_i = -K_i \frac{\partial h_i}{\partial x_i}, \quad (11)$$

where K_i is the permeability of the fracture.

By neglecting the velocity head, the relationship between total head h_i and the osmotic pressure P_i can be written as

$$P_i = (h_i - z_i) \rho_C g, \quad (12)$$

where h_i is the head distribution of the fracture and z_i is the position head of the fracture corresponding to the global coordinate system.

Taking a derivative of (12) yields the following equation:

$$\frac{\partial h_i}{\partial x_i} = \frac{1}{\rho_C g} \frac{\partial P_i}{\partial x_i} + \frac{\partial z_i}{\partial x_i} - \frac{P_i}{\rho_C^2 g} \frac{\partial \rho_C}{\partial x_i}. \quad (13)$$

Substituting (13) into (11) and then into (10), we obtain

$$\begin{aligned} \frac{\partial}{\partial x_i} \left[\frac{T_{fi}}{g} \left(\frac{\partial P_i}{\partial x_i} + \rho_C g \frac{\partial z_i}{\partial x_i} - \frac{P_i}{\rho_C} \frac{\partial \rho_C}{\partial x_i} \right) \right] dx_i \\ = \frac{\partial(\rho_C b_h dx_i)}{\partial t}, \end{aligned} \quad (14)$$

where T_{fi} is the transmissivity of fracture and x_i is the local coordinate of fracture.

During the fracture deformation process (closure/opening), the length of dx_i is unchanged, while the fluid density and fracture aperture vary. Equation (14) can be rewritten as

$$\frac{\partial(\rho_C b_h dx_i)}{\partial t} = \frac{\partial \rho_C}{\partial t} b_h dx_i + \frac{\partial b_h}{\partial t} \rho_C dx_i. \quad (15)$$

Assuming that the variation of fluid concentration is negligible, compression coefficient and the expansion coefficient of the fluid can be, respectively, written as [30]

$$\beta_P = \frac{1}{\rho_C} \frac{\partial \rho_{CP}}{\partial P}, \quad T \text{ is constant} \quad (16)$$

$$\beta_T = -\frac{1}{\rho_C} \frac{\partial \rho_{CT}}{\partial T}, \quad P \text{ is constant,}$$

where ρ_{CP} and ρ_{CT} , respectively, denote the variation of fluid density induced by external pressure P and temperature T . Therefore, the total variation of density can be described as

$$\frac{\partial \rho_C}{\partial t} = \frac{\partial \rho_{CP}}{\partial t} + \frac{\partial \rho_{CT}}{\partial t} = \rho_C \left(\beta_P \frac{\partial P}{\partial t} - \beta_T \frac{\partial T}{\partial t} \right). \quad (17)$$

The compression coefficient of the fracture can be written as

$$\alpha = -\frac{1}{b_h dx_i} \frac{\partial(b_h dx_i)}{\partial \sigma_{fne}}. \quad (18)$$

Since the fracture length does not vary with σ_{fne} , (18) can be rewritten as

$$\alpha = -\frac{1}{b_h} \frac{\partial b_h}{\partial \sigma_{fne}} = \frac{\delta_n}{b_h}, \quad (19)$$

where δ_n is the normal flexibility coefficient of the fracture, which can be written as

$$\delta_n = \frac{1}{k_n} = \frac{\partial \Delta V_j^c}{\partial \sigma_{fne}}. \quad (20)$$

When the external load is ensured, the total stress of the fracture will keep constant. The relationship between the effective normal stress and fluid pressure can be written as

$$d\sigma_{fne} = -dP_i. \quad (21)$$

Substituting (21) into (19), we obtain

$$\frac{\partial b_h}{\partial t} = \delta_n \frac{\partial P_i}{\partial t}. \quad (22)$$

Combination of (14), (15), (17), and (22) yields the following governing equation for fluid flow, expressed as

$$\begin{aligned} \rho_C g (b_h \beta_P + \delta_n) \frac{\partial P}{\partial t} \\ + \frac{\partial}{\partial x_i} \left[T_f \left(\frac{\partial P_i}{\partial x_i} + \rho_C g \frac{\partial z_i}{\partial x_i} - \frac{P_i}{\rho_C} \frac{\partial \rho_C}{\partial x_i} \right) \right] \\ = \rho_C g b_h \beta_T \frac{\partial T}{\partial t}. \end{aligned} \quad (23)$$

Assuming that b_h is equal to b_m and fluid flow through the fracture can be described using Darcy's law, permeability of the fracture can be written as

$$\begin{aligned} K_{fi} \\ = \frac{\rho_C g \left[(b_{m0}^2 k_{n0} + \sigma_{fne} (b_{m0} - 1)) / (b_{m0} k_{n0} + \sigma_{fne}) \right]^2}{12 \mu_C}. \end{aligned} \quad (24)$$

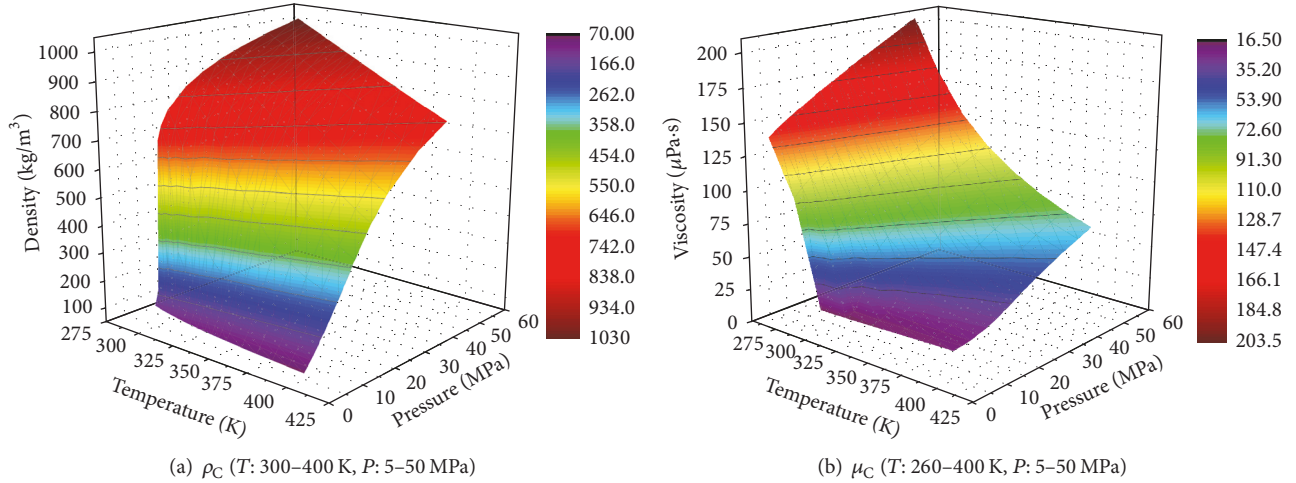


FIGURE 6: Variations of (a) density [17] and (b) dynamic viscosity [18] of supercritical CO₂ with the temperature and pressure.

The transmissivity can be written as

$$T_{fi} = K_{fi} b_{hi}$$

$$= \frac{\rho_C g [(b_{m0}^2 k_{n0} + \sigma_{fne} (b_{m0} - 1)) / (b_{m0} k_{n0} + \sigma_{fne})]^3}{12\mu_C}, \quad (25)$$

where μ_C is the dynamic viscosity of CO₂ and g presents the gravitational acceleration.

2.3. Governing Equation for Heat Conduction. The injection of CO₂ could result in variation of the temperature in caprock, which would then produce thermal stress [31]. Besides, the temperature alterations also lead to change of the physical properties of CO₂. Therefore, the temperature has a significant influence on permeability of the fracture. In this study, thermal effects produced by CO₂ flow through the fracture are neglected. Instead, the temperature of the injected CO₂ is regarded as a known condition which is imposed on the lower boundary of caprock. When the temperature of CO₂ is different from that of caprock, heat conduction phenomenon occurs. The governing equation can be written as

$$\frac{\partial T}{\partial t} = \frac{\lambda_s}{\rho_s c_s} \left(\frac{\partial^2 T}{\partial x^2} + \frac{\partial^2 T}{\partial y^2} \right), \quad (26)$$

where T denotes temperature variables and λ_s , c_s , and ρ_s , respectively, denote the heat conduction coefficient, heat capacity, and density of rock matrix.

2.4. Property Parameters of Supercritical CO₂. Property parameters of the supercritical CO₂ injected in the storage layer vary with the pressure and temperature. In this study, the density and dynamic viscosity of the supercritical CO₂ are, respectively, determined according to the empirical models put forward by Span and Wagner [17] and Vesovic et al. [18], as shown in Figure 6.

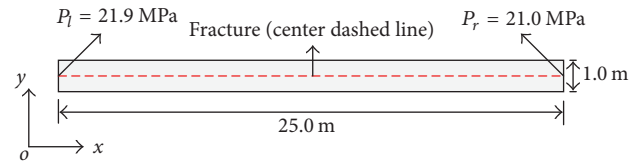


FIGURE 7: Validation model [19].

3. Coupled Model Validation

A 2D single fracture model, which has been studied before by Bower and Zyvoloski [19], is built and calculated to verify the effectiveness of the coupled model discussed above. For the coupled THM model in this study, the thermal field just plays a role in thermal stress within the rock matrix and property parameters of the fluid, with a clear physical process. Thus, we just make a comparison of the hydromechanical calculation results with those reported by Bower and Zyvoloski [19]. Numerical model is shown in Figure 7, with the input parameters listed in Table 1.

An initial stress field of $P_i = 21.0\text{ MPa}$ is imposed in both the matrix and fracture, and the initial fracture aperture is set to be $1 \times 10^{-5}\text{ m}$. The fluid is continuously injected in the fracture from the left side with $P_l = 21.9\text{ MPa}$, and P_r at right side is kept constant of 21.0 MPa . The left, upper and lower model boundaries are all displacement constraint. Normal stiffness of the fracture is kept unchanged of $1 \times 10^6\text{ MPa/m}$.

For this case, numerical and analytic solutions of aperture variation along the fracture length at $t = 500$ and 2000 days have been given by Bower and Zyvoloski [19]. The numerical results were calculated using the FEHM codes, and the analytic solutions were obtained using the method put forward by Wijesinghe [32]. Then, the fracture aperture was recalculated by solving the hydromechanical coupled model derived in this study with the COMSOL multiphysics. The comparison results are shown in Figure 8. To evaluate how

TABLE 1: Input parameters of the validation model [19].

Parameter	Value	Note
Length, m	25	Model
Width, m	1	
Density, kg/m ³	2716	Matrix
Young's modulus, MPa	1000	
Poisson's ratio	0.0	
Normal stiffness, MPa/m	1×10^6	
Porosity	1.0	
Initial aperture, m	1×10^{-5}	Fracture
Residual aperture, m	1×10^{-30}	
Maximum aperture, m	0.002	
Density, kg/m ³	1000	Fluid
Dynamic viscosity, Pa·s	0.001	
Compression coefficient, 1/Pa	0.0	

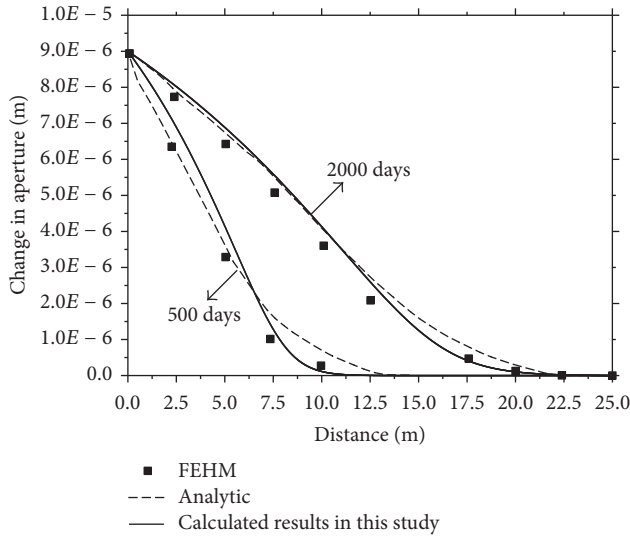


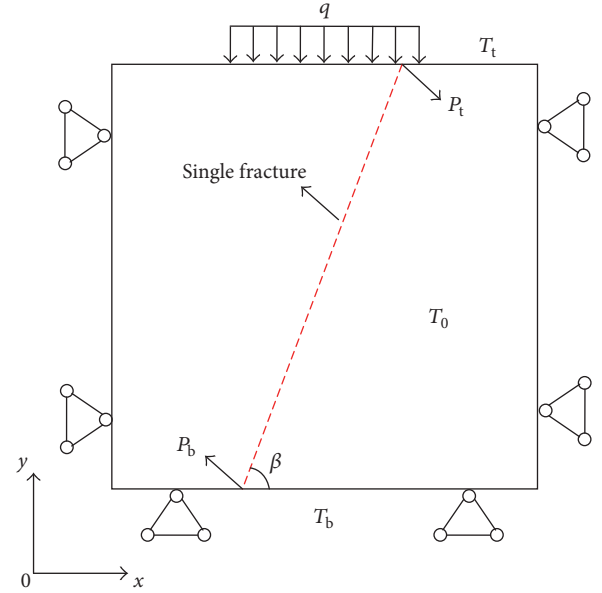
FIGURE 8: Comparison of analytic, numerical (FEHM) aperture [19] with the calculated results using COMSOL multiphysics in our study.

these curves fit well with each other, an evaluation coefficient μ is put forward [33]:

$$\mu = \sqrt{\frac{\sum_{i=1}^n (\Delta b_{hc} - \Delta b_{h2})^2}{n}}, \quad (27)$$

where n is the total number of measuring points, Δb_{hc} is the fracture aperture change calculated in our study, and Δb_{h2} refers to fracture aperture change calculated using other methods.

By using (27), μ between analytic solution and the calculated results in our study is only 3.36×10^{-7} and 1.63×10^{-7} m, respectively, at $t = 500$ and 2000 days. Besides, μ between the FEHM results and our results is only 3.79×10^{-7} and 3.18×10^{-7} m at $t = 500$ and 2000 days, respectively. Obviously, the calculation results agree well with the numerical and analytic

FIGURE 9: 2D conceptual model of a single fracture in caprock subjected to coupled THM effects, in which β denotes included angle between the fracture and horizontal direction, T_0 is the initial temperature of rock matrix, and T_b is equal to the temperature of injected CO_2 .

results of Bower and Zyvoloski [19], which indicates a good reliability of the coupled model in our study.

4. CO_2 Permeability Analysis of Single Fracture in Caprock

4.1. Model Setup. To quantitatively analyze permeability of the single fracture in caprock, a conceptual model is set up, as shown in Figure 9. The model is square with the size of $10 \text{ m} \times 10 \text{ m}$. The fracture connects the upper and lower model boundary and passes through the center position of the model. The right, left, and lower model boundary are displacement constraint. A vertical load of q is applied on the upper model boundary. Fluid pressure of P_b and P_t is, respectively, applied at the lower and upper side of the fracture. Temperature of T_b and T_t is imposed on the lower and upper model boundary. Input parameters are listed in Table 2.

4.2. Results and Discussion. First, variation of σ_{fne} , P_t , and T_f of the fracture, as well as ρ_C and μ_C of the supercritical CO_2 under THM coupled effects at different times for a vertical fracture ($\beta = 90^\circ$) were analyzed. Then, permeability of the fracture in caprock with respect to different q , P_b , b_{m0} , β , and T_b was, respectively, studied.

4.2.1. THM Coupled Effects on a Vertical Fracture. Boundary and initial conditions are as follows: $\beta = 90^\circ$, $b_{m0} = 0.5 \text{ mm}$, $q = 60 \text{ MPa}$, $P_b = 30 \text{ MPa}$, $P_t = 10 \text{ MPa}$, $T_b = 333.15 \text{ K}$, $T_t = 303.15 \text{ K}$, and $T_0 = 303.15 \text{ K}$.

TABLE 2: Parameters used in 2D THM coupled model.

Parameter	Value	Note
Density, kg/m^3	2500	Rock matrix
Young's modulus, GPa	100	
Poisson's ratio	0.3	
Heat conductivity, $\text{W}/(\text{m} \times \text{K})$	2.57	
Specific heat capacity, $\text{J}/(\text{m} \times \text{K})$	710	
Thermal expansion, $1/\text{K}$	6.0×10^{-7}	
Initial normal stiffness of fracture closure, GPa/m	60	Fracture
Normal stiffness of fracture opening, GPa/m	100	
Initial aperture, m	b_{m0}	
Residual aperture, m	1×10^{-6}	
Maximum aperture, m	0.002	
Fluid pressure at the lower side, MPa	P_b	
Fluid pressure at the upper side, MPa	P_t	Supercritical CO_2
Density, kg/m^3	Figure 6(a)	
Dynamic viscosity, Pa·s	Figure 6(b)	
Compression coefficient, $1/\text{Pa}$	Calculated with Figure 6(a)	
Thermal expansion, $1/\text{K}$	Calculated with Figure 6(b)	

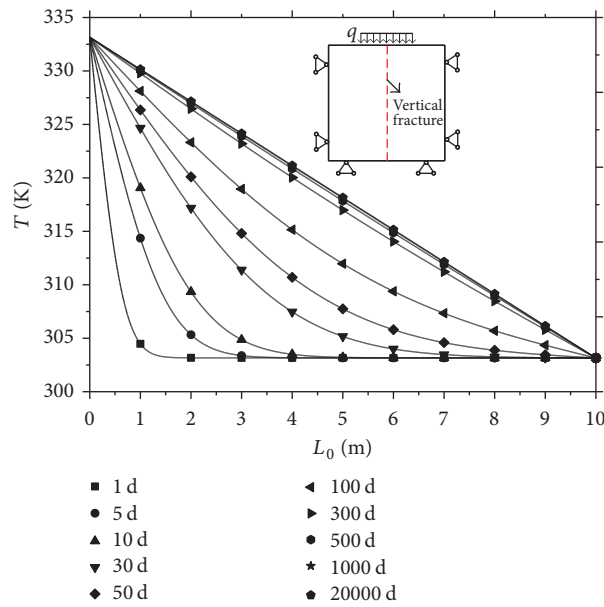


FIGURE 10: Temperature distribution along the fracture at different times.

At initial time, CO_2 was continuously injected in the fracture through the lower fracture side with a constant $P_b = 30 \text{ MPa}$. At different times, temperature distribution along the whole fracture length is shown in Figure 10, in which, x -axis (L_0) represents the distance from the measure point to the lower fracture tip along the fracture direction (in the range of 0–10 m). During the fluid flow test, heat conduction occurs in rock due to higher temperature of injected CO_2 (T_b) than that of the rock matrix (T_0). The heat transfers from high-temperature to the low-temperature position and finally approaches a stable state. From Figure 10, with the increase of time, heat at the lower fracture segment gradually transfers to the upper position until a stable state is achieved at $t = 300$ days.

During the heat conduction process, thermal expansion happens to the rock. Since both lateral boundaries (left and right) of the model are displacement constraint, the thermal expansion of rock leads to variation of normal stress in the fracture. Figures 11(a)–11(c), respectively, show σ_{fn} , P_f , and σ_{fne} along the fracture length at different times. By comparing Figures 10 and 11(a), generally, a high temperature in fracture corresponds to a high total normal stress, and a steady stress field is achieved when the thermal field is steady. Variation of σ_{fn} in the fracture with time results mainly from the thermal field.

Fluid pressure P_f in the fracture as a function of L_0 at different times is shown in Figure 11(b). With the increase of time, CO_2 flows along the direction of pressure drops,

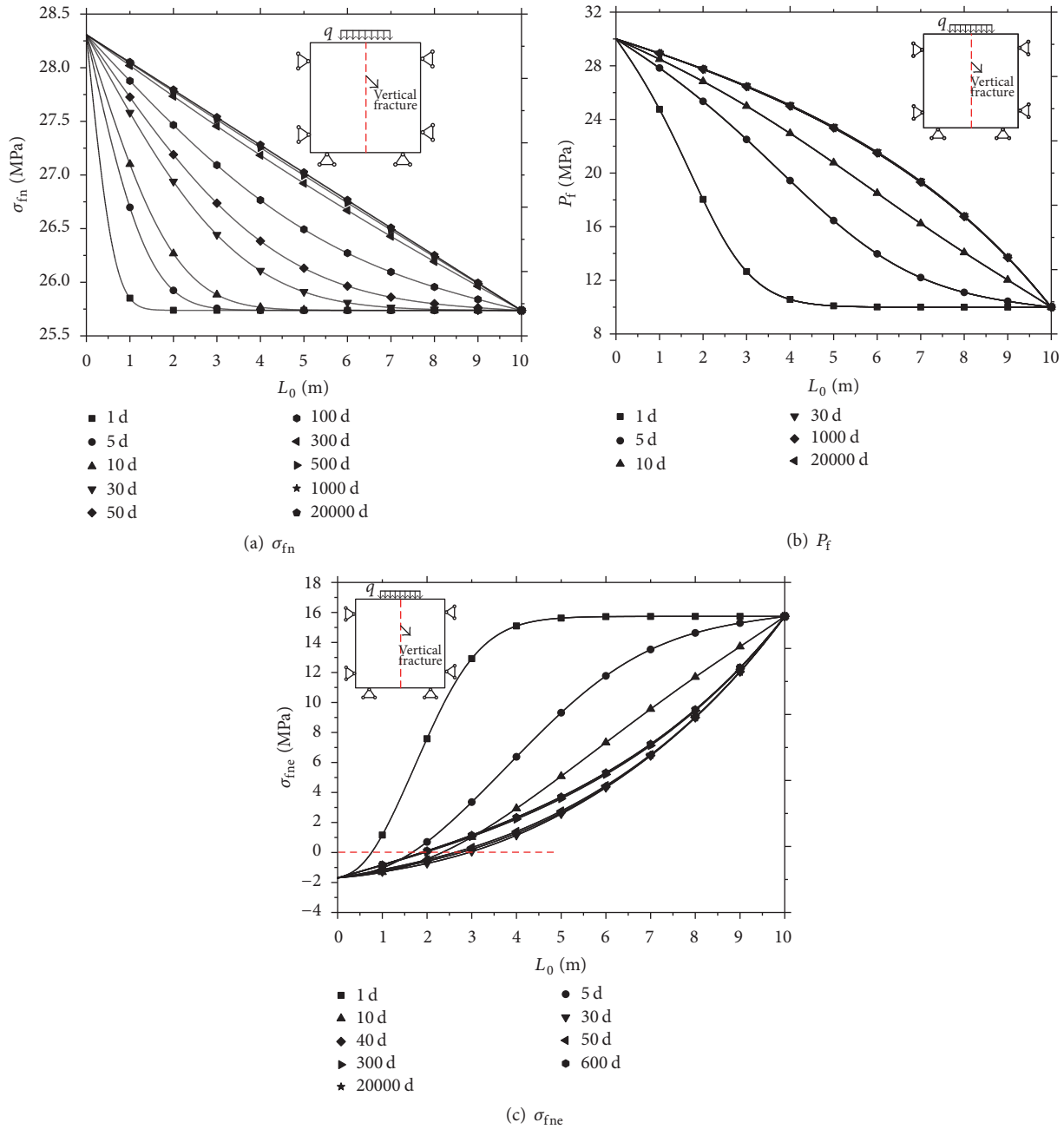


FIGURE 11: Distribution of (a) total normal stress, (b) fluid pressure, and (c) effective normal stress along the fracture at different times.

and, for this case, P_f reaches steady values at $t = 30$ days. By using (5), variation of σ_{fne} of the fracture at different times can be obtained (Figure 11(c)). In a certain small range of L_0 , P_f is larger than σ_{fn} , which results in negative values of σ_{fne} and a larger b_h than b_{m0} , as shown by the dashed line in Figures 11(c) and 12. Besides, σ_{fne} increases gradually as L_0 increases, which leads to corresponding decrease of b_h . It can also be seen from Figure 12 that, in the range of L_0 from 4 to 10 m, b_h first increases and then decreases, finally reaching stable values, as indicated by the red arrows. The main reason for this phenomenon is due to earlier stable state

of hydrodynamic field ($t = 30$ days) than that of the thermal field ($t = 300$ days).

Distribution of ρ_C and μ_C of the supercritical CO_2 along the fracture at different times is displayed in Figure 13. For $L_0 = 3-10$ m, both property parameters show an ascending-descending variation before attaining constant values, which are marked by the red arrows.

Under the coupled THM effects and taking variation of property parameters of CO_2 with different temperature and pressure into account, the transmissivity T_f of the fracture can be evaluated (Figure 14). Once hydrodynamic field of the fracture is stable, T_f will reach constant values.

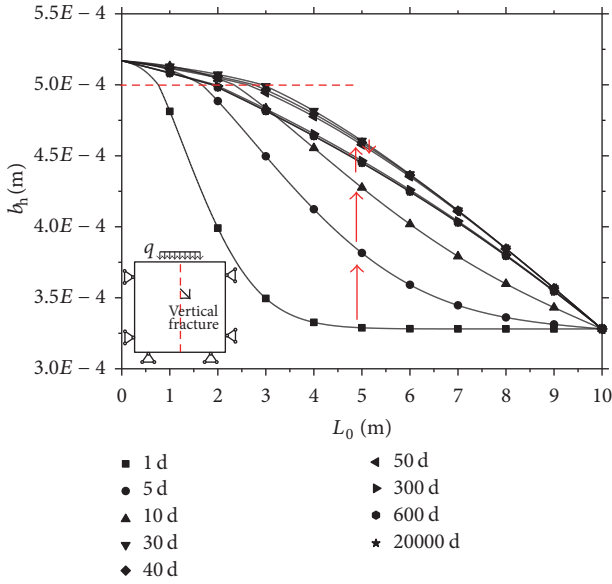


FIGURE 12: Variation of b_h along the fracture at different times.

4.2.2. Effect of Included Angle β . Due to complicated geological conditions of the caprock, included angle between fracture and the horizontal direction is various. Thus, it is of great significance to study the effect of β on permeability of the fracture under coupled THM effects. Six models with various β (45° , 51° , 59° , 68° , 79° , and 90°) were, respectively, set up. Boundary and initial conditions are as follows: $b_{m0} = 0.5$ mm, $q = 60$ MPa, $P_b = 20$ MPa, $P_t = 10$ MPa, $T_b = 333.15$ K, $T_t = 303.15$ K, and $T_0 = 303.15$ K. Other input parameters were the same as those listed in Table 2. Figure 15(a) presents variation of average T_f of the fracture with different β . With the increase of time, the average T_f increases gradually and then attains a constant value. Under coupled THM effects, the average T_f experiences an increasing trend with the increase of β . The average T_f of the fracture with included angle β of 45° , 51° , 59° , 68° , 79° , and 90° is 1.66×10^{-5} , 2.01×10^{-5} , 2.55×10^{-5} , 3.32×10^{-5} , 4.15×10^{-5} , and 4.55×10^{-5} m²/s. The average T_f for $\beta = 90^\circ$ increases by 1.74 times over that for $\beta = 45^\circ$, which indicates a weaker sequestration performance of caprock with a larger β .

4.2.3. Effect of Overburden Pressure q . When the storage layer of CO₂ is in different buried depths, the overburden pressure q of caprock is various, which would then largely impact the permeability of fracture. Six models with different q (30, 40, 50, 60, 70, and 80 MPa) were built. Boundary and initial conditions are as follows: $b_{m0} = 0.5$ mm, $\beta = 90^\circ$, $P_b = 30$ MPa, $P_t = 10$ MPa, $T_b = 333.15$ K, $T_t = 303.15$ K, and $T_0 = 303.15$ K. Average T_f of fracture for caprock with different q is displayed in Figure 15(b). With the increase of q from 30 to 80 MPa, T_f shows 3-4 orders of magnitude reduction, which corresponds to a gradually better sequestration performance of caprock.

4.2.4. Effect of Fluid Pressure Difference ΔP . For CO₂ sequestration in the storage layer, it is easier for CO₂ to diffuse with a larger inlet fluid pressure. However, a large inlet pressure would produce a large P_f to the fracture in caprock, which would then result in decrease of σ_{fne} and increase of fracture permeability. Six models with different fluid pressure difference ($\Delta P = 5, 10, 15, 20, 25,$ and 30 MPa) were, respectively, set up. ΔP denotes the difference between P_b and P_t . Boundary and initial conditions are as follows: $b_{m0} = 0.5$ mm, $q = 60$ MPa, $\beta = 90^\circ$, $P_t = 10$ MPa, $T_b = 333.15$ K, $T_t = 303.15$ K, and $T_0 = 303.15$ K. Variation of average T_f with different ΔP is shown in Figure 15(c). In the range of ΔP from 5 to 30 MPa, T_f in stable state shows an increase of 2-3 orders of magnitude.

4.2.5. Effect of Temperature T_C . Temperature T_C of the injected CO₂ also plays a role in permeability of fracture in caprock. Three models with different T_b (308.15, 328.15, and 353.15 K) were, respectively, built to analyze the effect of T_C . Both T_0 and T_t were set to be 308.15 K, with $b_{m0} = 0.5$ mm, $q = 60$ MPa, $\beta = 90^\circ$, $P_b = 30$ MPa, and $P_t = 10$ MPa. Calculation results are shown in Figure 15(d). It can be seen that the effect of T_b on average T_f of fracture is not as significant as that of β , q , and ΔP discussed above. Generally, when $T_b > T_0$, both σ_{fn} and b_h of fracture show an increasing trend. However, the results in Figure 15(d) show a relationship of T_f (328.15 K) $>$ T_f (308.15 K) $>$ T_f (353.15 K). This is because permeability of fracture is not only related to b_h but also related to property parameters of fluid under coupled THM effects.

4.2.6. Effect of Initial Aperture b_{m0} . From (25), T_f of fracture is closely related to b_{m0} . Four more models with different b_{m0} (0.05, 0.1, 0.3, and 0.5 mm) were set up to elucidate the effect of b_{m0} on permeability of fracture under coupled THM effects, with $q = 60$ MPa, $\beta = 90^\circ$, $P_b = 30$ MPa, $P_t = 10$ MPa, $T_b = 333.15$ K, $T_t = 303.15$ K, and $T_0 = 303.15$ K. T_f as a function of time with different b_{m0} is shown in Figure 15(e). Clearly, the larger b_{m0} , the larger average T_f . In the range of b_{m0} from 0.05 to 0.5 mm, the average T_f at stable state undergoes 4-5 orders of magnitude increase, which would then degrade the CO₂ sequestration performance. Besides, longer time is needed to attain a stable T_f with the decrease of b_{m0} , as indicated by the dashed lines.

5. Conclusions

In this study, a new coupled CO₂ flow, caprock deformation, and heat conduction finite element model is developed. A series of numerical calculations using COMSOL multiphysics software on caprock models with a single fracture subject to coupled THM effects were conducted. The main purpose is to elucidate the effect of fracture angle, overburden pressure, fluid pressure difference, injected CO₂ temperature, and the initial aperture on single fracture permeability in caprock. The conclusions can be drawn as follows.

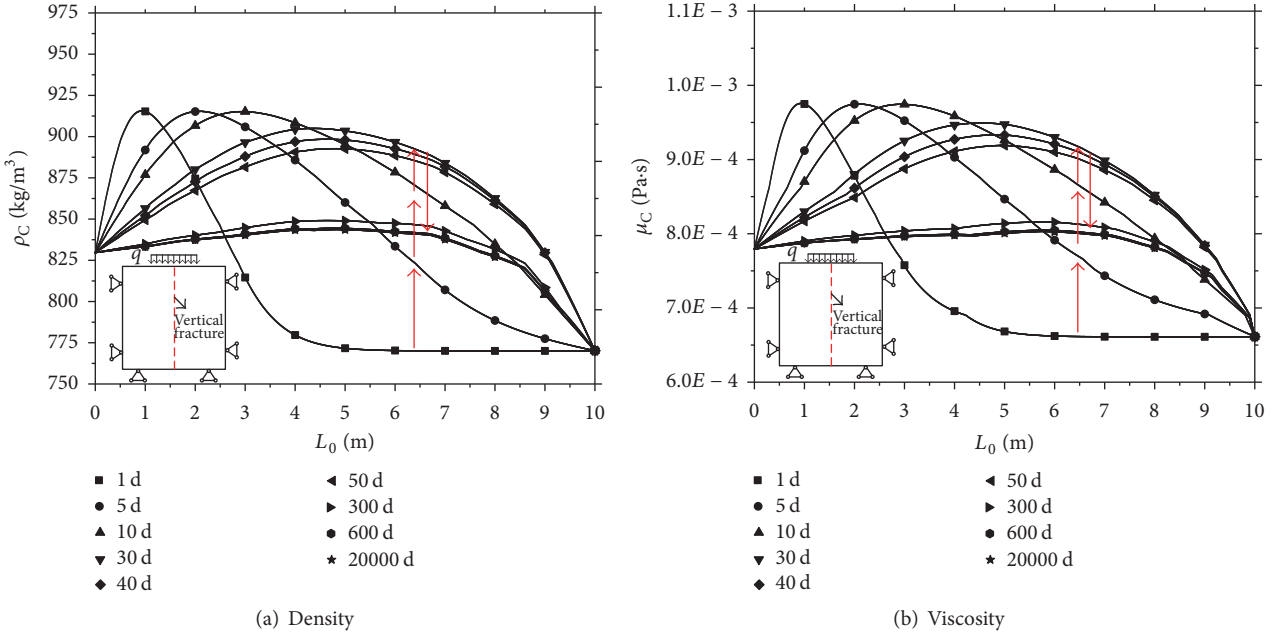


FIGURE 13: Variation of (a) density and (b) viscosity of supercritical CO₂ along the fracture at different times.

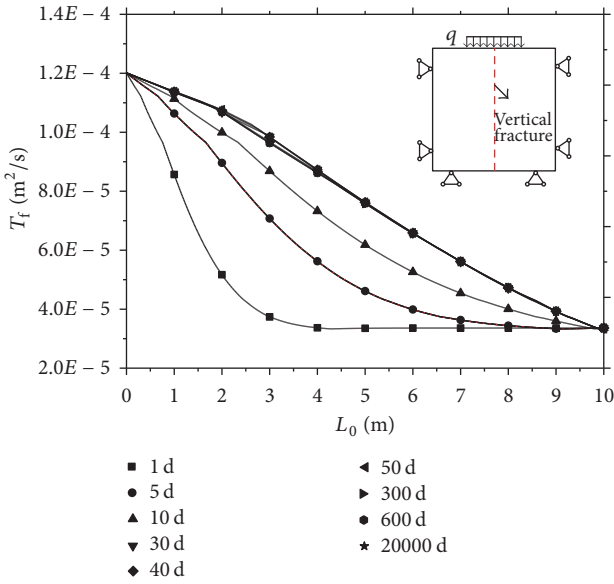


FIGURE 14: Transmissivity distribution along the fracture at different times.

(1) A 2D single fracture FE model has been applied to verify the performance of the new model under hydromechanical coupled effects. Variation of fracture aperture along the fracture length shows a good agreement compared with the numerical and analytic results of Bower and Zyvoloski [19], which indicates a good applicability of the new coupled model.

(2) For a vertical fracture under coupled THM effects, with the increase of time, heat in fracture achieves a stable state at $t = 300$ days, which corresponds to a steady stress state. CO₂ flows along the direction of pressure drops, and P_f reaches steady values at $t = 30$ days. With the increase of L_0 , σ_{fne} increases while b_h decreases gradually. For $L_0 = 3-10$ m, both ρ_C and μ_C of the supercritical CO₂ show an ascending-descending variation before attaining constant values.

(3) For all tested cases, with the increase of time, transmissivity T_f of fracture increases before approaches a stable value. With the increase of β , average T_f of fracture shows an increasing trend. T_f decreases with the increase of overburden pressure. In the range of fluid pressure difference from 5 to 30 MPa, stable T_f shows an increase of 2-3 orders of magnitude. T_f is less dependent on T_C of the injected CO₂ compared with that for initial aperture which shows 4-5 orders of magnitude increase in the range of b_{m0} from 0.05 to 0.5 mm.

We have tried in this paper to explain the coupled THM effects on transmissivity of a fracture in caprock. Clearly, more in-depth researches remain to be carried out on this issue. Our future works will focus on multiphase flow in fracture subjected to fully coupled THM processes to simulate the CO₂ sequestration in caprock. Besides, FE models of fracture networks will be set up and solved by the computational simulation methods.

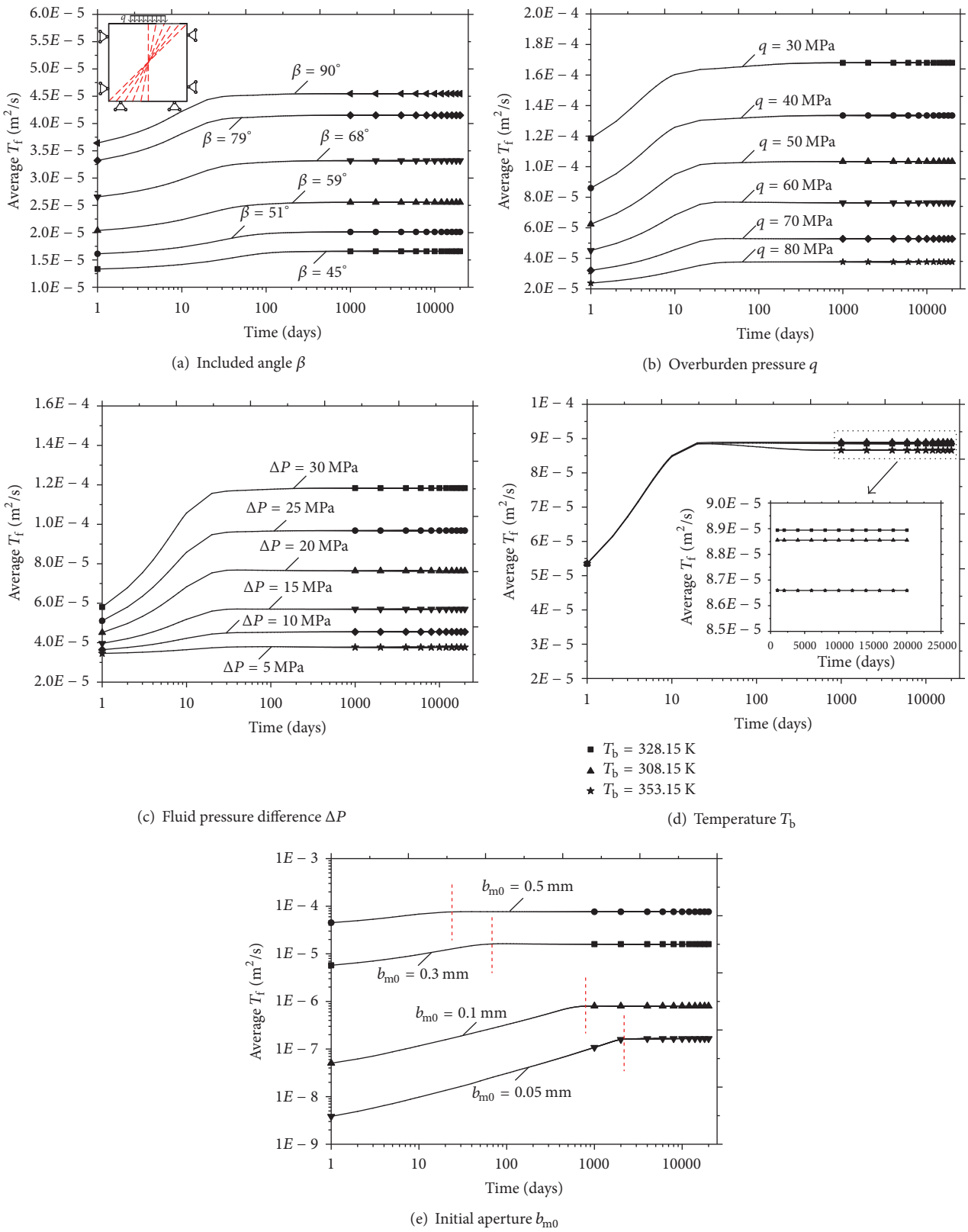


FIGURE 15: Effect of (a) included angle β , (b) overburden pressure q , (c) fluid pressure difference ΔP , (d) temperature T_b , and (e) initial aperture b_{m0} on average T_f of the fracture subject to coupled THM effects.

Conflicts of Interest

The authors declare that they have no competing interests regarding the publication of this paper.

Acknowledgments

The financial supports from the State Key Development Program for Basic Research of China (no. 2013CB036003), the Chinese Natural Science Foundation (no. 51374198), and the College Graduate Research and Innovation Projects of Jiangsu Province (KYLX15_1402) are gratefully acknowledged.

References

- [1] R. Shukla, P. Ranjith, A. Haque, and X. Choi, "A review of studies on CO₂ sequestration and caprock integrity," *Fuel*, vol. 89, no. 10, pp. 2651–2664, 2010.
- [2] D. Bolster, "The fluid mechanics of dissolution trapping in geologic storage of CO₂," *Journal of Fluid Mechanics*, vol. 740, no. 2, pp. 1–4, 2014.
- [3] H. E. Huppert and J. A. Neufeld, "The fluid mechanics of carbon dioxide sequestration," *Annual Review of Fluid Mechanics*, vol. 46, no. 46, pp. 255–272, 2014.
- [4] Z.-Q. Huang, P. H. Winterfeld, Y. Xiong, Y.-S. Wu, and J. Yao, "Parallel simulation of fully-coupled thermal-hydro-mechanical processes in CO₂ leakage through fluid-driven fracture zones," *International Journal of Greenhouse Gas Control*, vol. 34, pp. 39–51, 2015.
- [5] J. G. Wang, Y. Ju, F. Gao, Y. Peng, and Y. Gao, "Effect of CO₂ sorption-induced anisotropic swelling on caprock sealing efficiency," *Journal of Cleaner Production*, vol. 103, pp. 685–695, 2015.
- [6] J. Rutqvist and C.-F. Tsang, "A study of caprock hydromechanical changes associated with CO₂-injection into a brine formation," *Environmental Geology*, vol. 42, no. 2-3, pp. 296–305, 2002.
- [7] P. J. Armitage, R. H. Worden, D. R. Faulkner, A. C. Aplin, A. R. Butcher, and A. A. Espie, "Mercia mudstone formation caprock to carbon capture and storage sites: petrology and petrophysical characteristics," *Journal of the Geological Society*, vol. 170, no. 1, pp. 119–132, 2013.
- [8] A. P. Rinaldi, J. Rutqvist, and F. Cappa, "Geomechanical effects on CO₂ leakage through fault zones during large-scale underground injection," *International Journal of Greenhouse Gas Control*, vol. 20, pp. 117–131, 2014.
- [9] H. Lei, T. Xu, and G. Jin, "TOUGH2Biot—a simulator for coupled thermal-hydrodynamic-mechanical processes in subsurface flow systems: application to CO₂ geological storage and geothermal development," *Computers and Geosciences*, vol. 77, pp. 8–19, 2015.
- [10] J. E. Heath, T. A. Dewers, B. J. O. L. McPherson, M. B. Nemer, and P. G. Kotula, "Pore-lining phases and capillary breakthrough pressure of mudstone caprocks: sealing efficiency of geologic CO₂ storage sites," *International Journal of Greenhouse Gas Control*, vol. 11, no. 6, pp. 204–220, 2012.
- [11] K. Pruess, C. M. Oldenburg, and G. J. Moridis, *TOUGH2 User's Guide, Version 2.0*, Earth Science Division, Lawrence Berkeley National Laboratory, University of California, Berkeley, Calif, USA, 1999.
- [12] J. Rutqvist, Y.-S. Wu, C.-F. Tsang, and G. Bodvarsson, "A modeling approach for analysis of coupled multiphase fluid flow, heat transfer, and deformation in fractured porous rock," *International Journal of Rock Mechanics and Mining Sciences*, vol. 39, no. 4, pp. 429–442, 2002.
- [13] J. Taron, D. Elsworth, and K.-B. Min, "Numerical simulation of thermal-hydrologic-mechanical-chemical processes in deformable, fractured porous media," *International Journal of Rock Mechanics and Mining Sciences*, vol. 46, no. 5, pp. 842–854, 2009.
- [14] L. T. Hu, P. H. Winterfeld, P. Fakcharoenphol, and Y.-S. Wu, "A novel fully-coupled flow and geomechanics model in enhanced geothermal reservoirs," *Journal of Petroleum Science and Engineering*, vol. 107, pp. 1–11, 2013.
- [15] G. A. Zvyloski, B. A. Robinson, Z. V. Dash, and L. L. Trease, *Models and Methods Summary for the FEHM Application*, Los Alamos National Laboratory, 1996.
- [16] Q. Li, K. Ito, Z. Wu, C. S. Lowry, and S. P. Loheide II, "COMSOL multiphysics: a novel approach to ground water modeling," *Ground Water*, vol. 47, no. 4, pp. 480–487, 2009.
- [17] R. Span and W. Wagner, "A new equation of state for carbon dioxide covering the fluid region from the triple-point temperature to 1100 K at pressures up to 800 MPa," *Journal of Physical and Chemical Reference Data*, vol. 25, no. 6, pp. 1509–1596, 1996.
- [18] V. Vesovic, W. A. Wakeham, G. A. Olchowy, J. V. Sengers, J. T. R. Watson, and J. Millat, "The transport properties of carbon dioxide," *Journal of Physical and Chemical Reference Data*, vol. 19, no. 3, pp. 763–808, 1990.
- [19] K. M. Bower and G. Zvyloski, "A numerical model for thermo-hydro-mechanical coupling in fractured rock," *International Journal of Rock Mechanics and Mining Sciences*, vol. 34, no. 8, pp. 1201–1211, 1997.
- [20] T. Esaki, S. Du, Y. Mitani, K. Ikusada, and L. Jing, "Development of a shear-flow test apparatus and determination of coupled properties for a single rock joint," *International Journal of Rock Mechanics and Mining Sciences*, vol. 36, no. 5, pp. 641–650, 1999.
- [21] B. Li, Y. J. Jiang, T. Koyama, L. R. Jing, and Y. Tanabashi, "Experimental study of the hydro-mechanical behavior of rock joints using a parallel-plate model containing contact areas and artificial fractures," *International Journal of Rock Mechanics and Mining Sciences*, vol. 45, no. 3, pp. 362–375, 2008.
- [22] M. Javadi, M. Sharifzadeh, K. Shahriar, and Y. Mitani, "Critical Reynolds number for nonlinear flow through rough-walled fractures: the role of shear processes," *Water Resources Research*, vol. 50, no. 2, pp. 1789–1804, 2014.
- [23] G. Rong, J. Yang, L. Cheng, and C. B. Zhou, "Laboratory investigation of nonlinear flow characteristics in rough fractures during shear process," *Journal of Hydrology*, vol. 541, pp. 1385–1394, 2016.
- [24] N. Barton, S. Bandis, and K. Bakhtar, "Strength, deformation and conductivity coupling of rock joints," *International Journal of Rock Mechanics and Mining Sciences and*, vol. 22, no. 3, pp. 121–140, 1985.
- [25] K. G. Raven and J. E. Gale, "Water flow in a natural rock fracture as a function of stress and sample size," *International Journal of Rock Mechanics and Mining Sciences and*, vol. 22, no. 4, pp. 251–261, 1985.
- [26] W. B. Durham and B. P. Bonner, "Self-propping and fluid flow in slightly offset joints at high effective pressures," *Journal of Geophysical Research*, vol. 99, no. 5, pp. 9391–9399, 1994.

- [27] Z. Zhang and J. Nemcik, "Fluid flow regimes and nonlinear flow characteristics in deformable rock fractures," *Journal of Hydrology*, vol. 477, pp. 139–151, 2013.
- [28] X. Zhang and J. S. David, *Numerical Modelling and Analysis of Fluid Flow and Deformation of Fractured Rock Masses*, Pergamon, Oxford, UK, 2002.
- [29] S. C. Bandis, A. C. Lumsden, and N. R. Barton, "Fundamentals of rock joint deformation," *International Journal of Rock Mechanics and Mining Sciences & Geomechanics Abstracts*, vol. 20, no. 6, pp. 249–268, 1983.
- [30] J. Bear, *Dynamics of Fluids in Porous Media*, American Elsevier Publishing, New York, NY, USA, 1972.
- [31] K. Edlmann, S. Haszeldine, and C. I. McDermott, "Experimental investigation into the sealing capability of naturally fractured shale caprocks to supercritical carbon dioxide flow," *Environmental Earth Sciences*, vol. 70, no. 7, pp. 3393–3409, 2013.
- [32] A. M. Wijesinghe, *An Exact Similarity Solution for Coupled Deformation and Fluid Flow in Discrete Fractures*, Lawrence Livermore National Laboratory, Livermore, Calif, USA, 1986.
- [33] S.-Q. Yang, P. G. Ranjith, and Y.-L. Gui, "Experimental study of mechanical behavior and X-ray micro CT observations of sandstone under conventional triaxial compression," *Geotechnical Testing Journal*, vol. 38, no. 2, pp. 179–197, 2015.



Hindawi

Submit your manuscripts at
<https://www.hindawi.com>

